Acoustic confinement phenomena in oxide multifunctional nanophononic devices

A. E. Bruchhausen,[1,2,*] N. D. Lanzillotti-Kimura,[1,3,†] B. Jusserand,[4] A. Soukiassian,[5] L. Xie,[6,7] X. Q. Pan,[7] T. Dekorsy,[2,8] D. G. Schlom,[5,9] and A. Fainstein[1]

[1]*Centro Atómico Bariloche & Instituto Balseiro (C.N.E.A.) and CONICET, 8400 S. C. de Bariloche, R. N., Argentina*
[2]*Center for Applied Photonics and Department of Physics, University of Konstanz, D-78457 Konstanz, Germany*
[3]*Centre de Nanosciences et de Nanotechnologies, CNRS, Université Paris-Sud, Université Paris-Saclay, C2N, Avenue de la Vauve, 91120 Palaiseau, France*
[4]*Institut des NanoSciences de Paris, UMR 7588 C.N.R.S.-Université Pierre et Marie Curie, 75015 Paris, France*
[5]*Department of Materials Science and Engineering, Cornell University, Ithaca, New York 14853, USA*
[6]*National Laboratory of Solid State Microstructures and College of Engineering and Applied Sciences, Nanjing University, Nanjing 210093, People's Republic of China*
[7]*Department of Chemical Engineering and Materials Science, University of California Irvine, Irvine, California 92697, USA*
[8]*Institute of Technical Physics, German Aerospace Center (DLR), Pfaffenwaldring 38-40, 70569 Stuttgart, Germany*
[9]*Kavli Institute at Cornell for Nanoscale Science, Ithaca, New York 14853, USA*

(Received 1 December 2017; published 11 October 2018)

Engineering of phononic resonances in ferroelectric structures is a new knob to realize novel multifunctional devices. Here we show the possibility of predictively designing and fabricating phononic nanoresonators utilizing combinations of MBE-grown insulating ($BaTiO_3$, $SrTiO_3$) and metallic ($SrRuO_3$) oxides. We experimentally demonstrate the confinement of acoustic waves in the 100-GHz frequency range in a phonon nanocavity, and the the time and spatial beatings resulting from the coupling of two different hybrid nanocavities forming an acoustic molecule. Additionally, the direct measurement of Bloch-like oscillations of acoustic phonons is observed in a system formed by ten coupled resonators. Utilizing coherent phonon generation techniques, we study phonon dynamics directly in the time domain. The metallic $SrRuO_3$ layer introduces a local phonon generator and transducer that allows for the spatial, spectral, and time-domain monitoring of the complex generated waves. Our results introduce ferroelectric cavity systems as a new realm for the study of complex wave localization phenomena at the nanoscale. These systems can be successfully designed and conceived using state of the art growth techniques that combine perovskite oxides possessing multifunctional properties.

DOI: 10.1103/PhysRevMaterials.2.106002

I. INTRODUCTION

The study of complex localization phenomena requires direct access to spatial, temporal, and spectral information, which is not easily accessible in photonics and extremely challenging in electronics [1–6]. In this work, we unlock a new realm in the field of localization phenomena by using ferroelectric-based acoustic nanocavities as building blocks of complex structures.

Acoustic nanocavities [7–10] that confine and enhance phononic fields in the giga- and terahertz (GHz and THz, respectively) spectral range have been a subject of intense investigation for over a decade. The possibility of actually using acoustic phonons to control and modulate other excitations in solids, to process information, or to simulate other systems [11–15] has become the main motivation to investigate acoustic-phonon devices. An acoustic nanocavity is usually formed by two distributed Bragg reflectors (DBRs) enclosing an acoustic spacer [7], working in a similar way to how a classical Fabry-Perot interferometer works for light. Layers with thickness of a few nanometers, and atomically flat interfaces are two stringent requirements to fabricate devices capable of manipulating acoustic phonons in the GHz-THz range. A plethora of acoustic phonon devices have been experimentally demonstrated, ranging from acoustic mirrors and optimized filters [16] to complex coupled-cavity structures [15]. Conventional semiconductors [17–19] have usually been at the base of these devices mainly due to experience and maturity gained over the past few decades in the growth of such materials for electronics and optoelectronics applications. Nanocavities grown with other materials, such as ferroelectric and multifunctional oxides, have been less studied mainly due to the challenges of synthesizing heterostructures with the needed quality and interface precision. Despite this limitation, the superior acoustic performance and strong coupling between phonons, charge, and light of these materials has been recently demonstrated in acoustic superlattices, nanocavities, and other devices grown by reactive molecular-beam epitaxy (MBE) [8,20–22]. The use of ferroelectric materials in nanophononic applications paves the way towards novel devices where new interactions and transduction mechanisms can be engineered.

Acoustic phonons in the GHz-THz range lack commercial sources like the ones used for audible sound. Coherent acoustic-phonon generation techniques usually require

*axel.bruchhausen@cab.cnea.gov.ar
†daniel.kimura@c2n.upsaclay.fr

the use of pulsed lasers and a light/hypersound transducer [23–26]. The engineering and development of these transducers remains a major challenge in nanophononics. Metals like gold, nickel, and aluminum present excellent transduction capabilities in the near infrared (NIR) range [9,27–29] due to the photothermal coupling associated with large absorption coefficients. Conventional semiconductor and piezoelectric materials bring additional transduction mechanisms into the game, [25,27,30–33] and expand the application domains of nanophononics towards real electronic and optoelectronic devices. Interestingly, conventional semiconductor materials do not present the best possible phononic performance. $SrTiO_3$ (STO) has many properties that make it an attractive material for multifunctional-based material applications: it is a quantum paraelectric, it becomes superconducting at low temperatures (when highly doped), it can be used as a substrate for other multifunctional perovskites, it can be conductive or insulating depending on the dopants, etc. $BaTiO_3$ (BTO) is a standard ferroelectric with a Curie temperature that can be tuned up to 800 K by strain engineering [34]. Both, BTO and STO, are perovskite oxides that have optical gaps in the 350 nm wavelength (NUV) range, and thus, they are transparent in the near-infrared spectral range [21]. As such, they have a limited potential to be used as transducers using standard coherent phonon generation techniques. $SrRuO_3$ (SRO), on the other hand, is a metallic perovskite with a strong absorption of light in the NIR spectral range [35,36], enabling a strong and localized generation and detection of longitudinal acoustic phonons, with the interesting added value, with respect to prior work [9], that it can be epitaxially integrated with the aforementioned materials in the fabrication process.

In this work, we show the selective spatially localized impulsive generation and detection of acoustic phonons in a cavity based on a BTO/STO distributed Bragg reflector. We achieve spatially selective phonon generation and sensing by using SRO as the core layer of the cavity. Using high-speed asynchronous optical sampling (ASOPS) pump-probe spectroscopy [37–39], cavity dynamics can be clearly analyzed directly within the time domain. We also study the phonon dynamics of a coupled acoustic cavity system (the phononic equivalent of a hydrogen molecule) [11], where one of the cavity spacers was made of SRO. We report the direct observation of the time and spatial beatings in such an acoustic molecule. The generation of strain in one of the cavities, and the consequent exchange of elastic energy with the second cavity can be clearly observed. With these two simple structures we set the building blocks for the study of complex localization phenomena, such as Bloch oscillations [1].

Bloch oscillations [1] are one of the most striking quantum localization effects in solid state physics: an electron in a crystalline potential subject to a constant force will oscillate instead of being uniformly accelerated. In addition to electronics [40,41], Bloch oscillations have been reported in a series of systems including molecular systems [42], atoms in optical lattices [3], photonic [43], surface acoustic waves [44], and nanophononic [15] coupled cavity systems. By coupling a series of acoustic cavities, and introducing a gradient in the resonant frequencies, it is possible to mimic the effect in a nanophononic system [11,45]. We demonstrate the scalability of the structures studied by extending the use of SRO as a local transducer to a system composed of ten coupled acoustic nanocavities [11] in order to excite and measure Bloch-like oscillations of acoustic phonons in the 100-GHz range.

The paper is organized as follows. Section II is devoted to the study of a single hybrid cavity; Sec. III introduces the concept of a hybrid phononic molecule and presents the experimental study of the phonon dynamics in these structures. Results on Bloch oscillations of acoustic phonons in coupled cavity systems are presented in Sec. IV. Finally, in Sec. V, we conclude and present future perspectives.

II. HYBRID ACOUSTIC NANOCAVITIES

In this section, we introduce a device formed by a hybrid metal cavity (SRO) with a BTO/STO epitaxial oxide phonon mirror. A schematic of the structure is shown in Fig. 1(b).

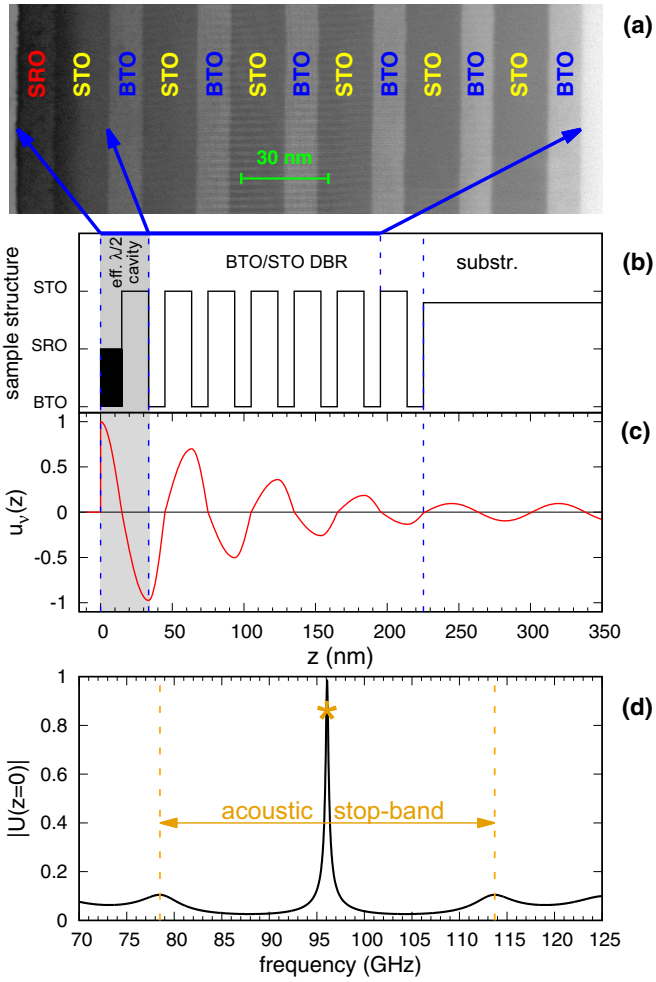

FIG. 1. Hybrid acoustic nanocavity structure. (a) Low-magnification HAADF-STEM image of the sample. (b) Schematics of the structure formed by a SRO acoustic spacer on top of a STO/BTO based DBR. The blue horizontal line at the top axis and the arrows mark the region shown in the image of (a). (c) Calculated displacement profile corresponding to the resonant mode. The maximum of the field is located at the top bilayer (SRO/STO). (d) Calculated surface displacement as a function of frequency; the double arrow indicates the extension of the acoustic mini-gap while the star marks the position of the resonant frequency.

The effective $\lambda/2$ cavity spacer is formed by a bilayer of SRO and STO. In this cavity structure, an acoustic mirror is formed by a phononic distributed Bragg reflector made of 6.5 bilayers of BTO_{26}/STO_{47}, where the subscripts indicate the number of unit cells of each material. The sample/air interface corresponds to a free surface boundary condition, resulting in total acoustic reflection, thus completing the cavity structure.

Figure 1(d) contains the calculated surface displacement as a function of the acoustic phonon frequency for vibrations incident from the substrate side with unit amplitude. The acoustic band gap is indicated with a double arrow. At the center of the stop band a confined mode can be distinguished, marked with a star. The atomic displacement profile inside the structure corresponding to the confined acoustic mode is shown in Fig. 1(c), where an exponentially evanescent decay of the displacement amplitude is observed along the extension of the DBR.

The hybrid nanocavity described in the previous paragraph was grown on a (110)-oriented $TbScO_3$ substrate by reactive-MBE. The resulting sample was characterized using high-angle annular dark-field scanning transmission electron microscopy (HAADF-STEM) [46] and XRD spectroscopy. A low-magnification image showing part of the grown structure is presented in Fig. 1(a). The thorough characterization revealed the samples to have sharp interfaces, and a deviation with respect to the nominal layers thickness of about ± 1 unit cell (see Appendix A for details).

The sample was experimentally studied by reflection-type pump-probe experiments at room temperature [24]. We used a high-speed asynchronous optical sampling (ASOPS) setup [37–39]. The ASOPS system is based on two femtosecond titanium:sapphire oscillators each providing 60 fs pulses at a $f_R = 0.8$ GHz repetition rate. The repetition rates are stabilized at a fixed frequency difference $\Delta f = 5$ kHz. For pump-probe experiments, one laser delivers the pump pulse generating coherent longitudinal-acoustic phonons, while the second one acts as a probe, sensing the instantaneous optical reflectivity of the sample, sampling the 1.25-ns-long time window. The pump and probe wavelengths are 785 and 830 nm, respectively. It is important to highlight that at these wavelengths both pump and probe beams only interact with the SRO layer, implying a spatially highly selective transduction. In other words, the phonons are generated and detected exclusively in the SRO layer. A typical incident pump (probe) laser power of 100 mW (10 mW) was used.

The top-left panel of Fig. 2 shows the transient optical reflectivity measured (black curves, E) on the hybrid nanocavity. This curve was obtained by subtracting the slowly varying components induced by the excited carriers and the temperature evolution of the sample [47]. A single-frequency oscillation decaying in time is observable. As we will discuss later, these oscillation corresponds to the acoustic phonons confined in the SRO/STO cavity spacer. The red line (T) corresponds to a simulation of the full pump-probe experiment based on a photoelastic interaction using an implementation of the transfer matrix method [48]. For this simulation, we assumed that (i) light absorption only occurs in the SRO and (ii) the photoelastic constant is nonzero only in the SRO. The simulations reproduce the time decaying behavior of the monochromatic signal remarkably well. By performing a

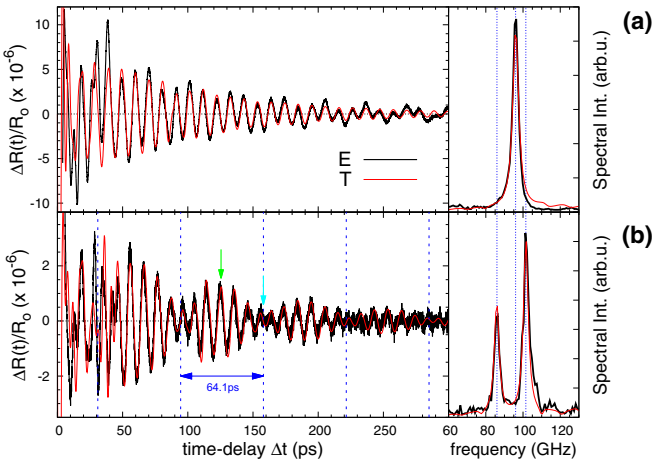

FIG. 2. Optical transient reflectivity of the hybrid phononic cavity (a) and molecule (b). Left panels present the measured (black) and simulated (red) signals using the ASOPS system. Slow varying components of the signals related to the electronic and thermal evolution of the sample were subtracted for clarity. Right panels show the Fourier transform of the measured and simulated time signals.

numerical Fourier transform of the extracted oscillations, it is possible to recover the frequencies of the phonons modulating the optical properties of the SRO layer. The right panel of Fig. 2(a) shows the Fourier transform amplitude where one clear peak is present in the spectrum. The peak at ∼96 GHz corresponds to the confined modes in the SRO cavity spacer. The red curve corresponds to the Fourier transform of the simulated signal in the left panel. The full width at half maximum (FWHM) of this cavity peak is ∼3 GHz, corresponding to an acoustic quality factor of $Q \sim 30$. As verified from comparison with the simulated spectra the Q factor, or equivalently its associated modes lifetime ($\tau_v \sim 100$ ps), is mainly limited by the transmission into the substrate, which is determined by the number of periods chosen for the DBR. Such confinement lifetimes and Q factors are comparable to results obtained for acoustic semiconductor nanocavities, measured by high-resolution Raman spectroscopy [49].

We have performed similar experiments on a nanocavity with the same sequence of layers, but without the SRO layer. In this case, *no* coherent phonons were observed when using infrared laser wavelengths due to the lack of an efficient local photoacoustic transducer. This confirms the essential role of the SRO layer as an efficient sub-THz phonon transducer compatible with high-quality epitaxial growth and the commensurate structure that results. It is also worth mentioning that an additional peak corresponding to the Brillouin mode exists at ∼30 GHz (not shown) [47], mainly originating in the massive transparent substrate and aided by the very small residual optical transmission of the SRO layer.

III. DYNAMICS IN PHONONIC MOLECULES

By coupling two identical cavities, it is possible to form the equivalent of an acoustic molecule [11]. In the phononic molecule, the modes of the two individual cavities hybridize to form two eigenstates of the full structure: one symmetric

and one antisymmetric with respect to the center of the molecule. Two aspects characterize the acoustic molecule: (i) the presence of these two acoustic modes and (ii) an elastic energy distribution of these two modes that is shared by the two cavity spacers. When the system is excited at one of its resonant energies, there is atomic displacement in both cavity spacers. By the same token, when one individual cavity spacer is excited, and since both modes have projections onto this cavity spacer region, the two eigenmodes of the molecule will be excited with a characteristic beating that is a fingerprint of a coupled mode. As we show below, the presence of the SRO layer allows for the localization of the phonon wave packet in both time and space.

In the phonon molecule structure studied, one of the cavities is a hybrid acoustic cavity similar to the one studied in the precedent section, while the second degenerate cavity is an oxide BTO/STO distributed Bragg reflector with a $\lambda/2$ BTO spacer. A schematic of the sample is shown in Fig. 3(a). The full structure consists on a SRO/STO cavity spacer, one intermediate DBR, a BTO cavity spacer, and a second DBR. This structure was epitaxially grown on a (110) $DyScO_3$ substrate, and its structural characterization revealed that the sample has sharp interfaces up to unit-cell abruptness (see Appendix A). Due to the high acoustic impedance mismatch between the BTO and the other two materials [8], only *one* period in the central DBR suffices to achieve a moderate coupling between the cavities. Again, the most important feature is that the generation and detection of the phononic effects is exclusively localized in the top cavity spacer, i.e., in the SRO cavity layer.

The calculated surface displacement for unit amplitude vibrations incident from the substrate as a function of energy is shown in Fig. 3(d). The double arrow indicates the extension of the acoustic mini-gap while the stars mark the spectral position of the resonant frequencies. Two clear modes at 85.9 and 101.5 GHz, symmetrically split from the uncoupled confined energy value 93.7 GHz, are observed inside the acoustic stop band. In Fig. 3(b), we show the simulated displacement profile corresponding to the two eigenmodes of the molecule. Note that the amplitude presents its maximum in the area of the acoustic cavity spacers and exponentially decays into the DBR towards the substrate. The opposite symmetry of the modes is also evident in the region of the second acoustic spacer (BTO). The simultaneous excitation of the two modes, as is the case in our experiments, results in a displacement profile where the elastic energy is mainly concentrated in one of the cavity spacers. The blue (red) curve in Fig. 3(c) presents the elastic energy distribution resulting from the coherent addition (subtraction) of the eigenmodes displacement profiles where the energy is mainly localized in the hybrid SRO/STO (or conversely the BTO) cavity layer, indicated by the corresponding shaded areas. It is worth emphasizing, that the eigenmode-subtraction has an extremely low weight at the SRO/STO cavity layer, whereas the eigenmode-addition has it maximal weight at the hybrid SRO/STO effective cavity layer.

The transient reflectivity curve measured on the hybrid molecule is shown in Fig. 2(b). A clear beating signal is observable, with a period of $\tau_R = 64.1$ ps. This signal decays in time as in the case of the single cavity structure studied in the previous section. The periodic signal corresponds to a

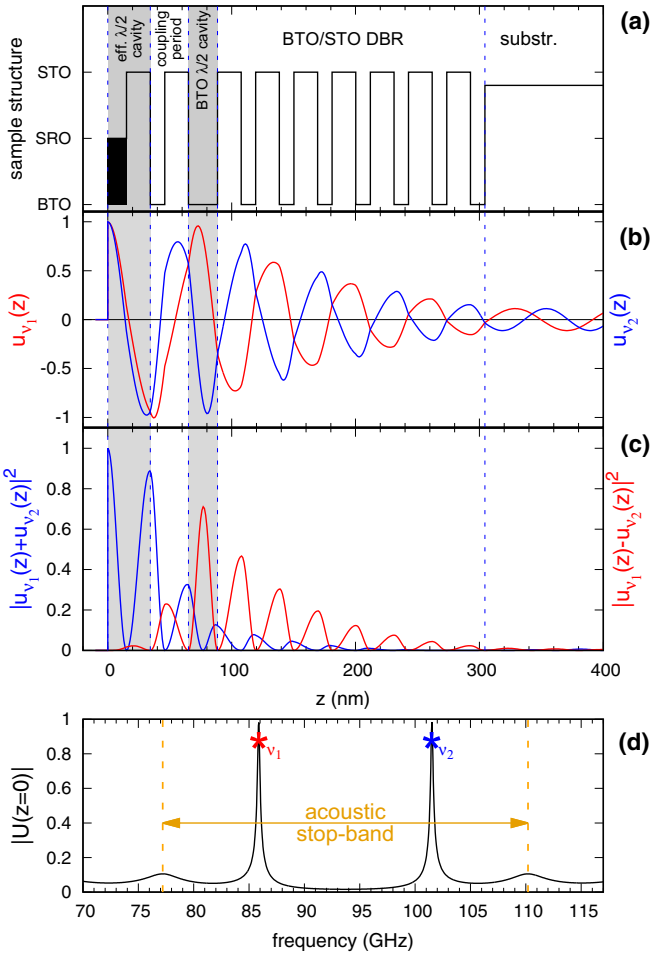

FIG. 3. Hybrid acoustic molecule. (a) Schematics of the phononic molecule formed by an air/spacer/DBR cavity and a DBR/spacer/DBR cavity. (b) Calculated displacement profile of the two resonant modes. Observe that the weight of the displacement is mainly located around the two molecule spacers. (c) Elastic energy distribution corresponding to the addition and subtraction of the two eigenmodes of the molecule. The blue (red) curve presents the energy localized in the hybrid SRO/STO (BTO) layer. (d) Calculated surface displacement as a function of energy, the double arrow indicates the extension of the acoustic minigap, while the stars mark the spectral position of the resonant frequencies.

phonon packet that spatially oscillates between the two cavity spacers, modulating the optical reflectivity of the SRO each time it reaches the surface cavity layer. It is the presence of this localized SRO transducer that allows the launch, and the locally probing of the wave-packet dynamics. In red, we present simulations of the pump-probe experiments that again reproduce the phonon dynamics in the molecule remarkably well. The Fourier transform of the measured (simulated) signal is shown in the right panel of Fig. 2(b) in black (red). Two clear peaks at 85.9 and 101.5 GHz are observable, which is the characteristic feature of the phononic molecule.

Figure 4 shows a simulation based on the transfer matrix method of the total acoustic displacement as a function of the spatial position (z) and time (t) corresponding to a localized generation in the SRO spacer at $t = 0$. We first study the case of the simple hybrid single cavity [Fig. 4(a)].

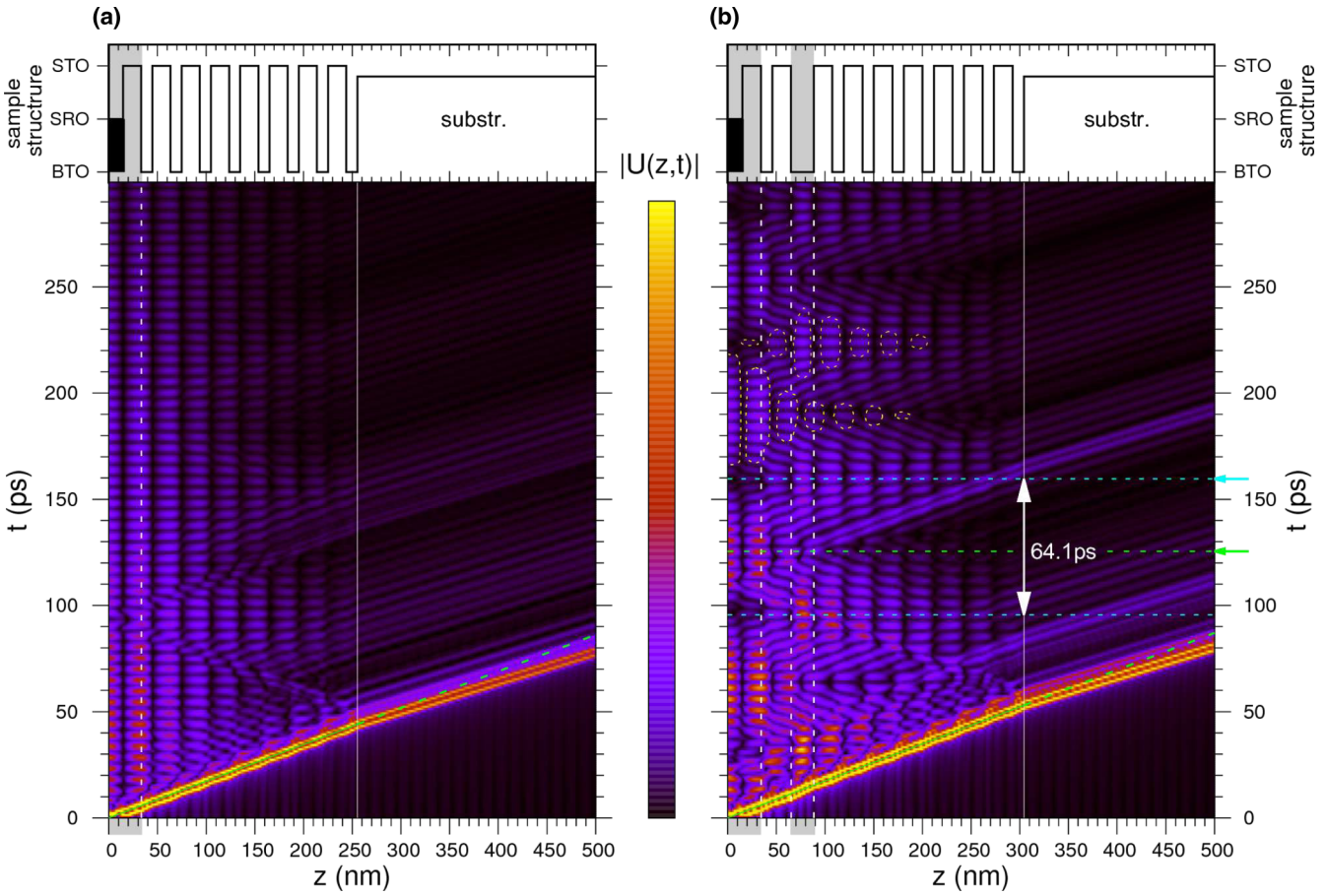

FIG. 4. Intensity map of the acoustic displacement in the hybrid devices as a function of the spatial position (z) and time (t) corresponding to a localized generation in the SRO spacer at $t = 0$. Brighter regions correspond to larger displacements. (a) Hybrid cavity structure case. (b) Phononic molecule case. The elastic energy oscillates between the two cavity spacers. The vertical double arrow indicates the period of the oscillation, while the dotted areas are guides to the eye showing the spatial distribution of the two localized modes.

After the first few picoseconds, where the displacement is only localized in the SRO layer, it is possible to distinguish the propagating pulselike component escaping towards the substrate. Only those phonons with the frequency of the cavity mode will remain trapped in the SRO/STO bilayer. A slow decay can be observed in the intensity of these cavity confined phonons. Note that in the pump-probe experiments only phonons present in the SRO layer produce a modulation of the optical reflectivity at the cavity mode frequency. The vertical white line indicates the interface between the substrate and the structure. The small change in the slope (see green-dotted lines) of the escaping acoustic pulse originates from the different effective speed of sound of the structure and the substrate. At this interface, due to the acoustic impedance mismatch, a weak part of the acoustic beam is reflected towards the air/sample interface.

The phonon dynamics in the molecule is analysed in Fig. 4(b). As is the case of the single hybrid cavity, we can identify the propagating pulselike component escaping towards the substrate. The remaining phonons show characteristic molecule beatings: the weight of the signal oscillates back and forth between the two spacers (located around 10 and 80 nm from the surface and indicated by the vertical dotted white lines) with a period of $\tau_R = 64.1$ ps. The inverse of this period, $\tau_R^{-1} = \nu_2 - \nu_1 = 15.69$ GHz, is proportional to the separation in frequency of both modes, and thus to the coupling strength between them. The horizontal arrows match the time of those displayed in Fig. 2(b) and correspond to the situation where the "pure" symmetric (green arrow) or antisymmetric (cyan arrow) mode combination is reached. By observing the intensity of the acoustic displacement at the top cavity layer it is possible to infer the periodic nature of the measured signal, demonstrating the importance of having a localized acoustic-phonon generator and detector in a complex structure. In this case, the SRO allowed the system to be prepared in a particular initial state and the beating of the molecule to be measured directly in the time domain using NIR pulsed lasers.

IV. BLOCH-LIKE OSCILLATIONS OF ACOUSTIC PHONONS

Bloch oscillations of a particle take place under the action of a periodic potential when a constant force is acting on it.

The application of a constant force results in the acceleration of the particle until it reaches the edge of the first Brillouin zone. At this point, Bragg scattering of the particle by the lattice potential takes place, flipping the sign of the particle velocity. In the Brillouin zone, the particle reappears in the other zone edge of the first Brillouin zone with a negative velocity. In real space, under a constant force the resulting motion of the particle is oscillatory instead of uniformly accelerated. This phenomenon was originally proposed by Bloch and Zener for electrons [1,50], and took some 60 years to be experimentally demonstrated [2,51–53]. In solid state physics the Wannier-Stark ladder is the spectral counterpart of Bloch oscillations, and is characterized by a series of equidistant eigenmodes.

The lack of charge of photons and phonons makes it difficult to define a photonic or phononic potential, respectively. A few years ago it was demonstrated that by concatenating a series of identical cavities it is possible to define a band [11]. The artificial band is centered on the energy of the individual cavities, the bandwidth is determined by the intercavity coupling, and two band gaps are created (lower and higher energy band gaps). It is also possible to mimic the effect of a potential by slightly detuning the energy of the individual cavities as a function of the position. The effect is equivalent to tilting the bands and band gaps. This strategy led to the experimental demonstration of Bloch oscillations of photons [43,45], phonons [15,54], and surface acoustic waves [44], among others. This information is essentially concentrated in the observation and measurement of the associated Wannier-Stark ladder. Direct access to spatial localization information and to the oscillation dynamics of phonon Bloch oscillations is, however, still missing. By scaling-up the engineering of coupled acoustic cavities, and by using the unique characteristics of the SRO as a local generator and detector of coherent acoustic phonons, we now show that it is possible to spatially localize the measurement of Bloch-like oscillations.

We present both measurements and theoretical simulations of a system composed of ten coupled acoustic cavity structures supporting Bloch-like spatial oscillations of acoustic phonons. Each cavity consists of a $\lambda/2$ spacer and a single $\lambda/4$ BTO layer acting as an interference mirror, as shown in Fig. 5(a). The first cavity spacer is made of SRO/STO, while the other nine spacers are made of STO. The structure was designed to present a nominal energy gradient of $\sim$10 GHz/cavity, starting with the SRO/STO cavity at 75 GHz. As in the cases of the single hybrid cavity and the phononic molecule, the sample was grown by reactive-MBE on a (110) $DyScO_3$ substrate.

Figure 5(b) shows the calculated surface displacement profile as a function of phonon energy. The rich spectrum shows regular peaks between 60 and 110 GHz, and a second series of peaks between 120 and 220 GHz. Each peak corresponds to a phononic mode with the energy mainly localized between the air-sample interface, which acts as a perfect mirror and the region in space where coherent Bragg interference takes place. Note that this effect can be described in terms of tilted effective bands for the acoustic phonons as discussed in Appendix B.

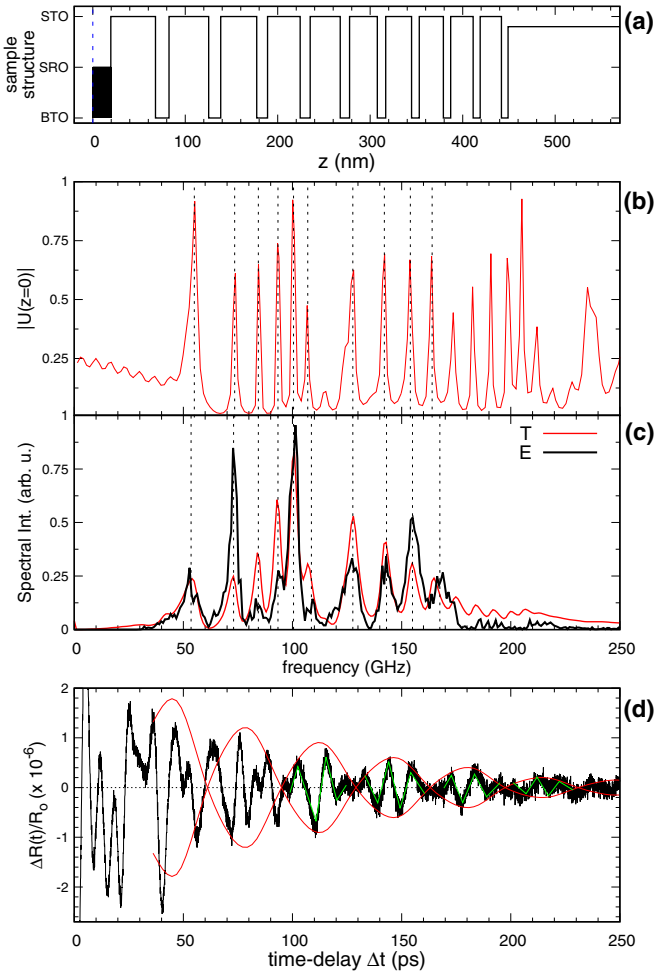

FIG. 5. Bloch oscillations of acoustic phonons in hybrid complex structures. (a) Schematics of the phononic multiple-cavity resonator formed by a series of concatenated cavities with a gradient in the individual resonant energy. The first cavity is an air/spacer/DBR cavity. (b) Surface displacement as a function of frequency. Note the series of peaks corresponding to the acoustic Wannier-Stark ladder. (c) Fourier transforms of the measured (black) and simulated (red) optical transient reflectivity signals. (d) Measured (black) optical transient reflectivity signal. The red lines are a guide to the eye to indicate the oscillations corresponding to the acoustic wave packet reaching the SRO layers.

The measured optical transient reflectivity signal is shown in black in Fig. 5(d). The slowly varying signal corresponding to the thermal and electronic evolution of the metal was removed for clarity. Well defined oscillations with decaying amplitude in time can be observed that last for more than $\sim$200 ps. This decay in amplitude is mainly attributed to transmission into the substrate as in the previous cases. The SRO layer provides a unique means to measure time-resolved localized strains, allowing us, to measure the oscillations of complex acoustic phonon waves in the time domain. This same structure is also a local phonon generator, launching the acoustic phonons from a particular element in the array of phononic resonators.

Fourier transforms of both the measured (black) and simulated (red) signals are shown in Fig. 5(c). A rich and complex Stark-ladder-like spectrum can be observed, and most of the measured peaks can be associated to the surface displacement peaks of Fig. 5(b). The agreement between the simulated and the measured spectra is remarkable. These are Wannier-Stark ladderlike modes.

When the modes of the Wannier-Stark ladderlike feature are excited from the SRO cavity, the acoustic phonons will propagate until they reach the region on the sample matching a Bragg condition where they will be reflected, changing the sign of the phonon velocity. When the phonons reach the surface, they are reflected changing the sign of the oscillation. This perfect reflection can be seen as an antisymmetric boundary condition: in this way, the full Bloch-like oscillation will be completed with a second round trip to the Bragg-condition zone of the sample. In Fig. 5(d), the red and green lines are a guide to the eye to indicate the Bloch-like behavior of the detected signal, with a period of approximately ∼65 ps. Each maximum corresponds to the arrival time of the phonon wave packet at the SRO layer, the only place where they can be detected. Also noteworthy is the inversion of the signal that occurs in each detected period [indicated with green lines in Fig. 5(d)], in full agreement with the total reflection suffered by the wave-packet at the surface of the sample.

V. CONCLUSIONS

Using picosecond ultrahigh frequency acoustics and local transducers we have demonstrated that it is possible to access the full information characterizing complex wave localization phenomena, a unique feature as compared with photons and electrons. Additionally, GHz acoustic phonons provide a unique way to couple to other relevant excitations in solids, for example, spins, two-level systems, and polaritons, all relevant to novel quantum information technologies.

By employing a surface SRO cavity, we generated confined acoustic phonons. The metallic character of the SRO allowed us to selectively generate and monitor spatially localized acoustic phonons in the technologically relevant 100-GHz frequency range, paving the way to study novel materials in nanophononics. This structure was used as a building block to design a double cavity system, where a surface SRO cavity was coupled to a BTO cavity, forming a phononic molecule. The selective spatial excitation of confined acoustic phonons allowed us to experimentally localize the generated complex waves and thus study the coupling dynamics between the two acoustic-phonon resonators. Phonons were generated exclusively in the SRO cavity, and then the energy was transferred from the SRO and the BTO cavities. The beating dynamics between two modes of a molecule has been clearly observed in the time domain. In the last section of this work, we introduced a system formed by one hybrid acoustic nanocavity coupled to an array of nine cavities. Such a system is able to support Bloch-like acoustic-phonon oscillations. We experimentally showed that phononic modes trapped between the air-sample interface and the bandgaps resulting from the coupling of the nanocavity modes can generate spatial oscillations of the acoustic phonons when excited from the metallic surface. The direct access to spatial and time domain dynamics unveils for the first time the full wave function behavior in these resonator-based structures. The potential of incorporating SRO as a light/hypersound transducer inside STO/BTO structures thus constitutes one of the first steps towards the engineering of new nano-optophononic applications involving complex structures and the study of localized light-charge-phonon interactions.

ACKNOWLEDGMENTS

A.E.B. acknowledges the Alexander von Humboldt Foundation (Bonn, Germany) for financial support. N.D.L.-K. acknowledges support from European Research Council (ERC) Starting Grant No. 715939, Nanophennec. This work is partially supported by the Ministry of Science and Technology (Argentina) through ANPCyT grant Nos. PICT2011-1718, PICT2012-1661 and PICT2013-2047, by the Deutsche Forschungsgemeinschaft (DFG) through the SFB767, and by the Ministry of Science, Research and Arts of Baden-Württemberg (Germany).

A.E.B. and N.D.L.-K. contributed equally to this work.

APPENDIX A: SAMPLE CHARACTERIZATION USING XRD SPECTROSCOPY AND STEM

The samples were grown by reactive molecular-beam epitaxy (reactive-MBE), that enables the precise and commensurate growth of insulating perovskite oxides such as $SrTiO_3$ (STO) and $BaTiO_3$ (BTO), together with metallic oxides such as $SrRuO_3$ (SRO). Each sample has been carefully characterized. As an example, in Fig. 6 we show a $\theta - 2\theta$ x-ray diffraction scan of the hybrid acoustic nanocavity grown on a (110)-oriented $TbScO_3$ substrate. The red stars (∗) indicate the

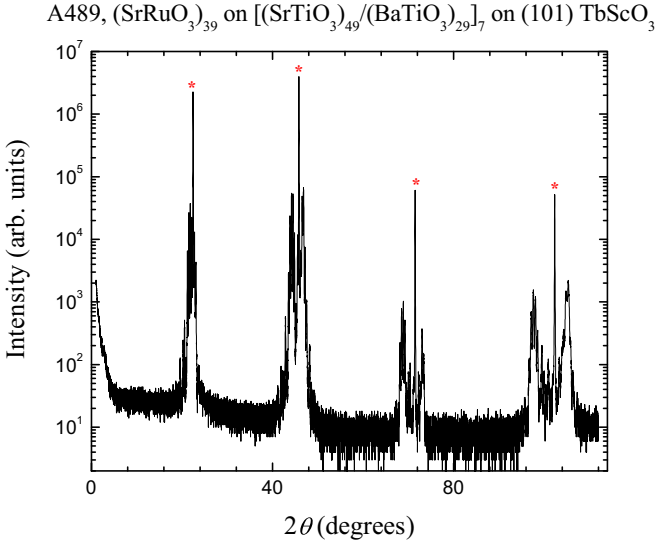

FIG. 6. $\theta - 2\theta$ x-ray diffraction pattern of the hybrid acoustic nanocavity. The red stars (∗) indicate the peaks diffracted from the substrate, (110)-oriented $TbScO_3$ in this case.

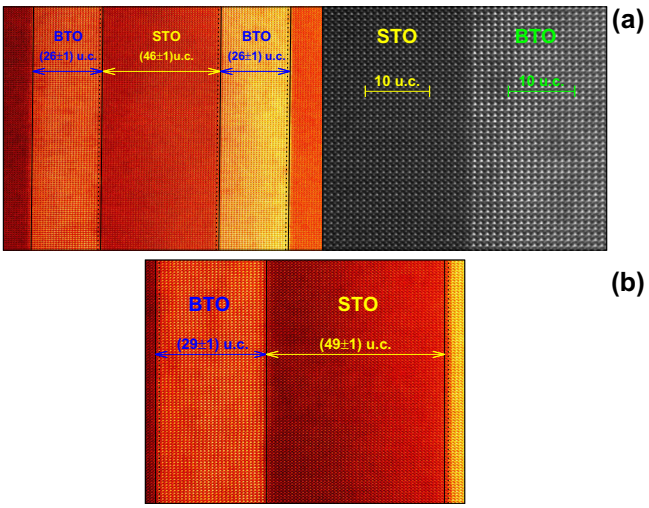

FIG. 7. High resolution HAADF-STEM images. The columns of atoms for each material can be observed. As an example, the interfaces of the layers are indicated by the vertical lines, and the result from counting the unit cells is indicated. (a) corresponds to the simple hybrid nanocavity. On the right a high magnification image is presented for a characteristic STO-BTO interface, where the sharp edge between materials is evident. The slightly larger unit cell in the BTO relative to the STO can also be resolved here. (b) corresponds to the acoustic phonon molecule structure.

diffraction peaks resulting from the substrate. Satellite peaks are originated by the diffraction from the oxide heterostructure, which has a total thickness of about 225 nm.

Structural characterization is not only important to establish the outstanding quality, interface abruptness, and layer thicknesses of the reactive-MBE grown structure, but it is also essential to test the models that are used for the sample design and those used to performed the simulations, which describe the interaction processes and the acoustic phonon dynamics in these heterostructures. Precise determination of the width of each individual layer was performed using high-angle annular dark-field scanning transmission microscopy (HAADF-STEM) [46], which provides atomic resolution. Using the latter technique, the meticulous counting of the number of unit cells (u.c.) for *each* of the grown layers was performed. Figure 7 shows high-magnification HAADF-STEM images that exemplify the procedure under which the number of unit cells (u.c.), within each layer of all three samples, was obtained. Panel (a) corresponds to the hybrid nanocavity, where the left image shows one and a half periods of the BTO/STO acoustic distributed Bragg reflector (DBR), and the image on the right shows the close up view of a STO-BTO interface with clear resolution at the unit cell level. Panel (b) shows one DBR period of the hybrid acoustic phonon molecule. This thorough characterization enabled the precise determination of the number of unit cells for each layer, and the error was estimated to be of about ± 1 u.c.

In Fig. 8, low magnification HAADF-STEM images are compared to the corresponding sketch of the structure of each sample. In each layer the material, either STO or BTO, is indicated and the subscripts indicate the determined number of unit cells. The region of the samples shown in each image is delimited by the arrows and is indicated by the horizontal thick red line at the top axis of the sketches. Panel (a) corresponds to the hybrid acoustic molecule (coupled acoustic cavities), and (b) to the sample displaying Bloch-like oscillations. The sketches are the same as those presented in Figs. 3(a) and 5(a), respectively.

APPENDIX B: ACOUSTIC BLOCH OSCILLATIONS

The sample displaying Bloch oscillations is the most complex of all three, not only with respect to its design, but also due to the difficulty of its growth. Here we are dealing with several layers with thicknesses that need to be carefully matched and achieved in order to obtain the desired effect. As explained in the text, the sample is formed by the stacking of 10 coupled effective $\lambda/2$ cavities of STO, each with its corresponding acoustic mirror. Given the extremely high impedance mismatch of these oxides, a difference with respect to devices proposed using, e.g., semiconductor materials [11], is that only a single $\lambda/4$ BTO layer is enough to act as an interference mirror. The nominal frequency gradient between cavities was designed to be of the order of $\sim$10 GHz/cavity. The experimental gradient, as derived from the individual layer characterization using HAADF-STEM, discussed in Appendix A, turned out to be slightly lower and of (9 ± 1) GHz/cavity, remarkably close to the value of our design.

Figure 9(b) shows the effective acoustic potential achieved by this structure [11,45], i.e., allowed energy band diagram. This energy band structure represents, for each cavity number, what would be the mini-bands and mini-gaps of an infinite system composed of identical cavities. As such, they are not the real band structures of the system, but useful illustrations. The mini-band originating from the nanocavity confined states is the central black one. The bands are tilted as a function of cavity number (#) reflecting the effective linear potential that has been introduced. The allowed mini-band is bounded by forbidden regions at higher and lower energies, indicated by the yellow areas. We will refer to these latter regions, as upper and lower mini-gap bands, respectively. The purpose of such a scheme is to emphasize the spatial dependence of the modes which vary linearly in the case shown, and is useful to define what are, roughly speaking, the allowed energies. Cavity #1 corresponds to the SRO cavity, and #10 to the one just above the substrate. As was previously discussed for a single cavity, the surface of the sample acts as a perfect broadband mirror for the acoustic phonons.

By comparing Fig. 9(b) with Fig. 9(c) [same as Fig. 5(c)], we can assign the peaks between 75 and 120 GHz to acoustic phonons trapped between the air-sample interface and the low-energy stop-band of the couple-cavity system, and the second family of peaks between 125 GHz and 170 GHz to acoustic phonons trapped between the air-sample interface and the high-energy stop-band of the couple-cavity system [55].

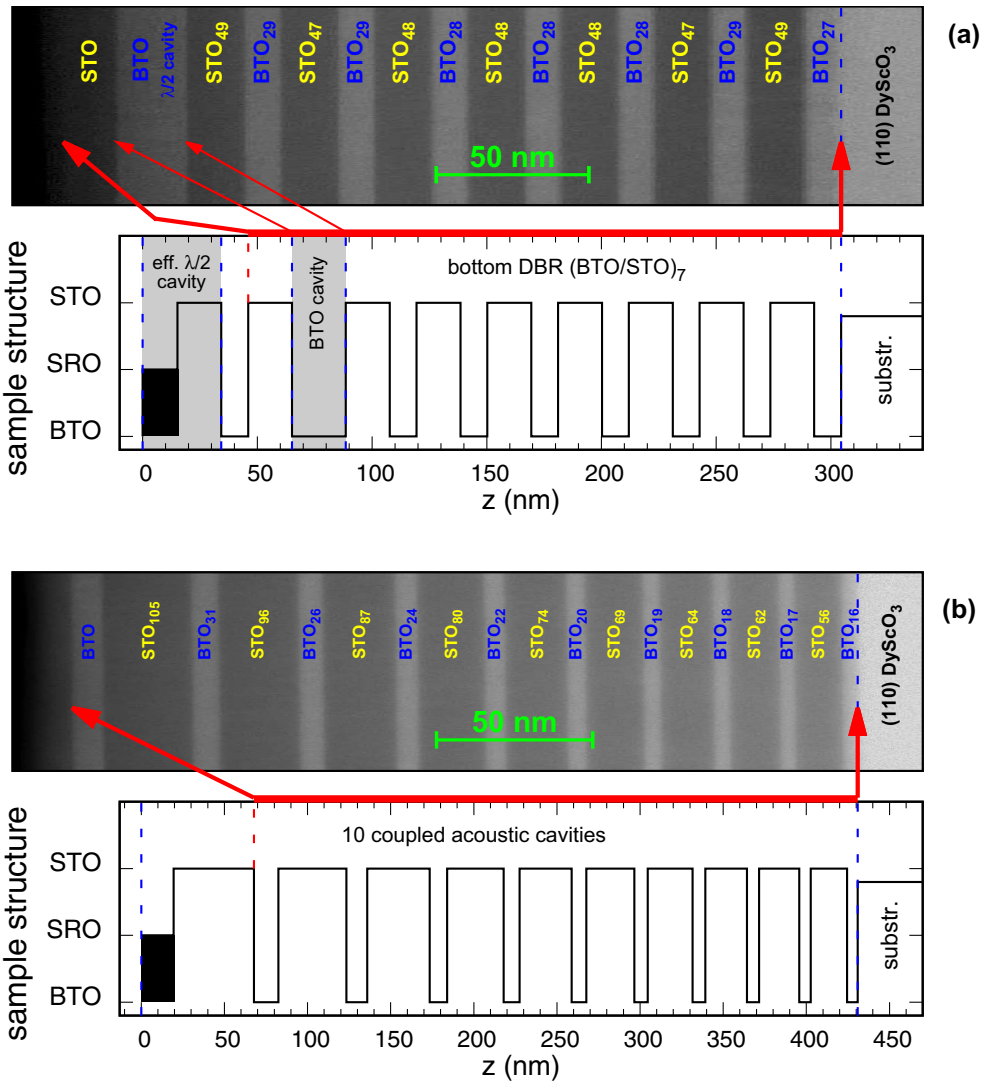

FIG. 8. Low magnification HAADF-STEM images, showing how the "counting" of the unit cells (u.c.) in each individual layer is accounted for. The sub-indices correspond to the number of u.c. counted. (a) corresponds to the phonon molecule, i.e., two coupled cavities, and (b) to the sample displaying Bloch-like oscillations. At the bottom of each panel a sketch of each sample is depicted. The red tick line at the top axis indicates the part of the sample that is displayed in the HAADF-STEM image above.

When these modes of the Wannier-Stark ladder are excited from the SRO cavity, the acoustic phonons will propagate until they reach the region on the sample matching a Bragg condition where they will be reflected, changing the sign of the particle velocity; this region coincides, to a first order of approximation, with the presence of the upper or lower band gaps. When the phonons reach the surface, they are reflected, changing the sign of the oscillation. This antisymmetric boundary condition is essential to observe the Bloch-like oscillatory behavior. A major difference between our results and previously reported phononic Bloch oscillations is the period. For prior results it is not only determined by the energy difference between neighbor cavities, but approximately twice this value, because the phonons are not trapped between two band gaps.

For completeness, we also show for this sample the comparison between experiments and theory in the time domain. In Fig. 9(a) the corresponding experimental temporal trace in black [same as in Fig. 5(d)], and the simulated curve in red and vertically shifted for clarity, are reproduced. As can be well noticed, the overall agreement of experiment and theory is remarkable.

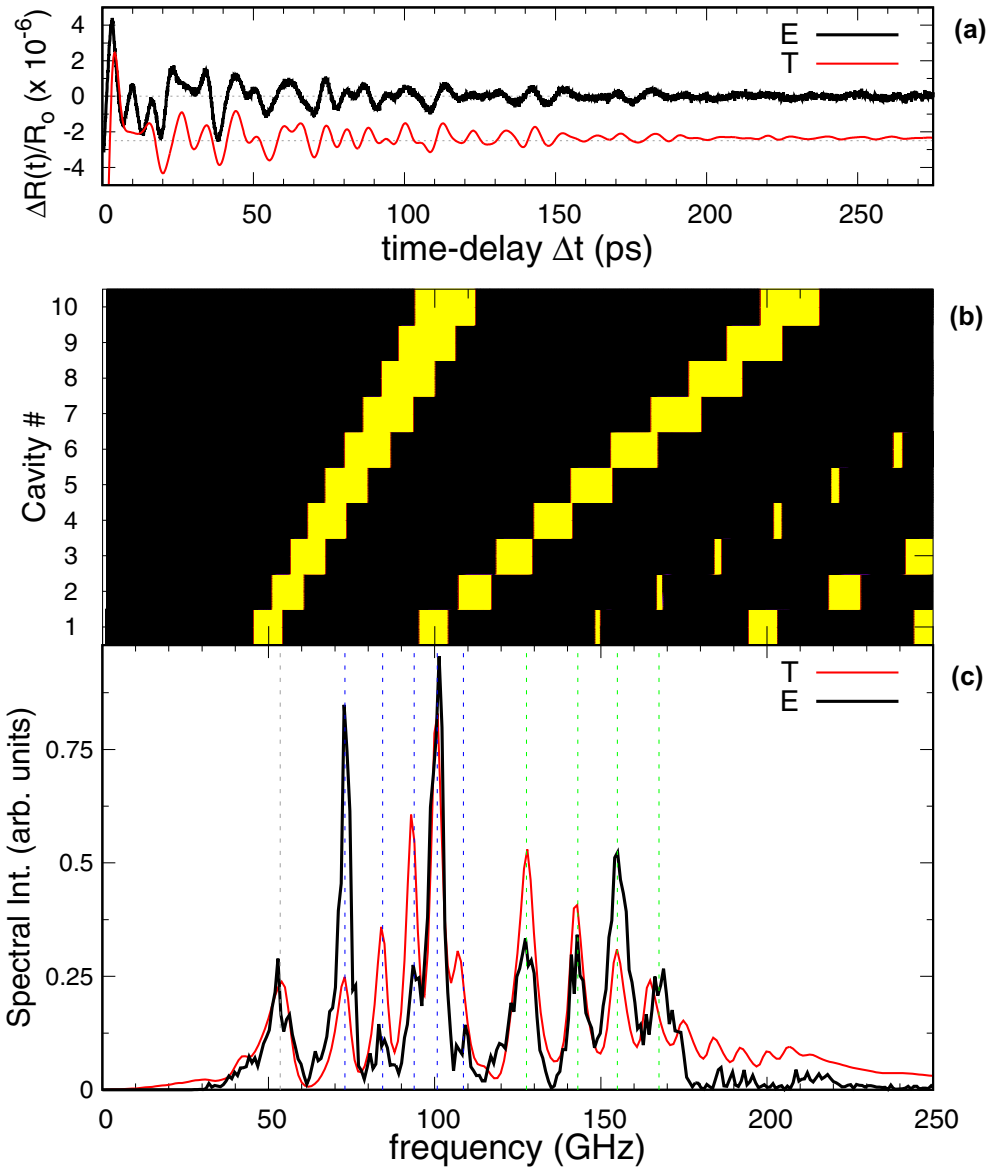

FIG. 9. Details of the sample displaying acoustic Bloch oscillations: (a) compares the experimental (E) and calculated (T) transient oscillations of the probes reflectivity that result due to the presence of the acoustic Wannier-Stark ladder-like modes. The theoretical red curve is vertically down shifted. (b) corresponds to the effective acoustic potential as a function of the acoustic frequency for the system formed by 10 coupled acoustic cavities with a frequency gradient of ∼10 GHz/cavity. (c) plots the nFT of the corresponding transients of panel (a). The vertical dashed lines match the frequency of the experimental peaks.

[1] F. Bloch, Über die Quantenmechanic de Elektronen in Kristallgittern, Z. Phys. **52**, 555 (1928).

[2] K. Leo, P. H. Bolivar, F. Brüggemann, R. Schwedler, and K. Köhler, Observation of Bloch oscillations in a semiconductor superlattice, Solid State Commun. **84**, 943 (1992).

[3] M. B. Dahan, E. Peik, J. Reichel, Y. Castin, and C. Salomon, Bloch Oscillations of Atoms in an Optical Potential, Phys. Rev. Lett. **76**, 4508 (1996).

[4] T. Pertsch, P. Dannberg, W. Elflein, A. Bräuer, and F. Lederer, Optical Bloch Oscillations in Temperature Tuned Waveguide Arrays, Phys. Rev. Lett. **83**, 4752 (1999).

[5] R. Morandotti, U. Peschel, J. S. Aitchison, H. S. Eisenberg, and Y. Silberberg, Experimental Observation of Linear and Nonlinear Optical Bloc Oscillations, Phys. Rev. Lett. **83**, 4756 (1999).

[6] A. R. Kolovsky and H. J. Korsch, Bloch oscillations of cold atoms in two-dimensional optical lattices, Phys. Rev. A **67**, 063601 (2003).

[7] M. Trigo, A. Bruchhausen, A. Fainstein, B. Jusserand, and V. Thierry-Mieg, Confinement of Acoustical Vibrations in a Semiconductor Planar Phonon Cavity, Phys. Rev. Lett. **89**, 227402 (2002).

[8] A. Soukiassian, W. Tian, D. A. Tenne, X. X. Xi, D. G. Schlom, N. D. Lanzillotti-Kimura, A. Bruchhausen, A. Fainstein, H. P. Sun, X. Q. Pan, A. Cros, and A. Cantarero, Acoustic Bragg mirrors and cavities made using piezoelectric oxides, Appl. Phys. Lett. **90**, 042909 (2007).

[9] N. D. Lanzillotti-Kimura, A. Fainstein, B. Perrin, B. Jusserand, A. Soukiassian, X. X. Xi, and D. G. Schlom, Enhancement and Inhibition of Coherent Phonon Emission of a Ni Film in a $BaTiO_3/SrTiO_3$ Cavity, Phys. Rev. Lett. **104**, 187402 (2010).

[10] S. Anguiano, A. E. Bruchhausen, B. Jusserand, I. Favero, F. R. Lamberti, L. Lanco, I. Sagnes, A. Lemaître, N. D. Lanzillotti-Kimura, P. Senellart, and A. Fainstein, Micropillar Resonators for Optomechanics in the Extremely High 19–95-GHz Frequency Range, Phys. Rev. Lett. **118**, 263901 (2017).

[11] N. D. Lanzillotti-Kimura, A. Fainstein, C. A. Balseiro, and B. Jusserand, Phonon engineering with acoustic nanocavities: Theoretical considerations on phonon molecules, band structures, and acoustic Bloch oscillations, Phys. Rev. B **75**, 024301 (2007).

[12] T. Berstermann, C. Brüggemann, M. Bombeck, A. V. Akimov, D. R. Yakovlev, C. Kruse, D. Hommel, and M. Bayer, Optical bandpass switching by modulating a microcavity using ultrafast acoustics, Phys. Rev. B **81**, 085316 (2010).

[13] T. Berstermann, A. V. Scherbakov, A. V. Akimov, D. R. Yakovlev, N. A. Gippius, B. A. Glavin, I. Sagnes, J. Bloch, and M. Bayer, Terahertz polariton sidebands generated by ultrafast strain pulses in an optical semiconductor microcavity, Phys. Rev. B **80**, 075301 (2009).

[14] J. V. Jäger, A. V. Scherbakov, B. A. Glavin, A. S. Salasyuk, R. P. Campion, A. W. Rushforth, D. R. Yakovlev, A. V. Akimov, and M. Bayer, Resonant driving of magnetization precession in a ferromagnetic layer by coherent monochromatic phonons, Phys. Rev. B **92**, 020404 (2015).

[15] N. D. Lanzillotti-Kimura, A. Fainstein, B. Perrin, B. Jusserand, O. Mauguin, L. Largeau, and A. Lemaître, Bloch Oscillations of THz Acoustic Phonons in Coupled Nanocavity Structures, Phys. Rev. Lett. **104**, 197402 (2010).

[16] N. D. Lanzillotti-Kimura, B. Perrin, A. Fainstein, B. Jusserand, and A. Lemaître, Nanophononic thin-film filters and mirrors studied by picosecond ultrasonics, Appl. Phys. Lett. **96**, 053101 (2010).

[17] Ü. Özgür, Chang-Won Lee, and H. O. Everitt, Control of Coherent Acoustic Phonons in Semiconductor Quantum Wells, Phys. Rev. Lett. **86**, 5604 (2001).

[18] J. Wang, Y. Hashimoto, J. Kono, A. Oiwa, H. Munekata, G. D. Sanders, and C. J. Stanton, Propagating coherent acoustic phonon wave packets in $In_xMn_{1-x}As/GaSb$, Phys. Rev. B **72**, 153311 (2005).

[19] Y. Ezzahri, S. Grauby, J. M. Rampnoux, H. Michel, G. Pernot, W. Claeys, S. Dilhaire, C. Rossignol, G. Zeng, and A. Shakouri, Coherent phonons in Si/SiGe superlattices, Phys. Rev. B **75**, 195309 (2007).

[20] A. Bruchhausen, A. Fainstein, A. Soukiassian, D. G. Schlom, X. X. Xi, M. Bernhagen, P. Reiche, and R. Uecker, Ferroelectricity-Induced Coupling between Light and Terahertz-Frequency Acoustic Phonons in $BaTiO_3/SrTiO_3$ Superlattices, Phys. Rev. Lett. **101**, 197402 (2008).

[21] D. A. Tenne, A. Bruchhausen, N. D. Lanzillotti-Kimura, A. Fainstein, R. S. Katiyar, A. Cantarero, A. Soukiassian, V. Vaithyanathan, J. H. Haeni, W. Tian, D. G. Schlom, K. J. Choi, D. M. Kim, C. B. Eom, H. P. Sun, X. Q. Pan, Y. L. Li, L. Q. Chen, Q. X. Jia, S. M. Nakhmanson, K. M. Rabe, and X. X. Xi, Probing nanoscale ferroelectricity by ultraviolet Raman spectroscopy, Science **313**, 1614 (2006).

[22] U. Kumar Bhaskar, N. Banerjee, A. Abdollahi, Z. Wang, D. G. Schlom, G. Rijnders, and G. Catalan, A flexoelectric microelectromechanical system on silicon, Nat. Nanotech. **11**, 263 (2016).

[23] C. Thomsen, J. Strait, Z. Vardeny, H. J. Maris, J. Tauc, and J. J. Hauser, Coherent Phonon Generation and Detection by Picosecond Light Pulses, Phys. Rev. Lett. **53**, 989 (1984).

[24] C. Thomsen, H. T. Grahn, H. J. Maris, and J. Tauc, Surface generation and detection of phonons by picosecond light pulses, Phys. Rev. B **34**, 4129 (1986).

[25] C.-K. Sun, J.-C. Liang, and X.-Y. Yu, Coherent Acoustic Phonon Oscillations in Semiconductor Multiple Quantum Wells with Piezoelectric Fields, Phys. Rev. Lett. **84**, 179 (2000).

[26] F. Della Picca, R. Berte, M. Rahmani, P. Albella, J. M. Bujjamer, M. Poblet, E. Cortés, S. A. Maier, and A. V. Bragas, Tailored hypersound generation in single plasmonic nanoantennas, Nano Lett. **16**, 1428 (2016).

[27] A. Huynh, N. D. Lanzillotti-Kimura, B. Jusserand, B. Perrin, A. Fainstein, M. F. Pascual-Winter, E. Peronne, and A. Lemaître, Subterahertz Phonon Dynamics in Acoustic Nanocavities, Phys. Rev. Lett. **97**, 115502 (2006).

[28] P. Ruello, A. Ayouch, G. Vaudel, T. Pezeril, N. Delorme, S. Sato, K. Kimura, and V. E. Gusev, Ultrafast acousto-plasmonics in gold nanoparticle superlattices, Phys. Rev. B **92**, 174304 (2015).

[29] K. O'Brien, N. D. Lanzillotti-Kimura, J. Rho, H. Suchowski, X. Yin, and X. Zhang, Ultrafast acousto-plasmonic control and sensing in complex nanostructures, Nat. Commun. **5**, 4042 (2014).

[30] G. Rozas, M. F. Pascual Winter, A. Fainstein, B. Jusserand, P. O. Vaccaro, S. Saravanan, and N. Saito, Piezoelectric semiconductor acoustic cavities, Phys. Rev. B **72**, 035331 (2005).

[31] O. Matsuda, O. B. Wright, D. H. Hurley, V. Gusev, and K. Shimizu, Coherent shear phonon generation and detection with picosecond laser acoustics, Phys. Rev. B **77**, 224110 (2008).

[32] W. Maryam, A. V. Akimov, R. P. Campion, and A. J. Kent, Dynamics of a vertical cavity quantum cascade phonon laser structure, Nat. Commun. **4**, 2184 (2013).

[33] C. Brüggemann, A. V. Akimov, A. V. Scherbakov, M. Bombeck, C. Schneider, S. Höfling, A. Forchel, D. R. Yakovlev, and M. Bayer, Laser mode feeding by shaking quantum dots in a planar microcavity, Nat. Photonics **6**, 30 (2012).

[34] K. J. Choi, M. Biegalski, Y. L. Li, A. Sharan, J. Schubert, R. Uecker, P. Reiche, Y. B. Chen, X. Q. Pan, V. Gopalan, L.-Q. Chen, D. G. Schlom, and C. B. Eom, Enhancement of ferroelectricity in strained $BaTiO_3$ thin films, Science **306**, 1005 (2004).

[35] L. Braic, N. Vasilantonakis, B. Zou, S. A. Maier, N. McN. Alford, A. V. Zayats, and P. K. Petrov, Optimizing strontium ruthenate thin films for near-infrared plasmonic applications, Sci. Rep. **5**, 9118 (2015).

[36] P. Kostic, Y. Okada, N. C. Collins, Z. Schlesinger, J. W. Reiner, L. Klein, A. Kapitulnik, T. H. Geballe, and M. R. Beasley,

Non-Fermi-Liquid Behavior of $SrRuO_3$: Evidence from Infrared Conductivity, Phys. Rev. Lett. **81**, 2498 (1998).

[37] A. Bartels, F. Hudert, C. Janke, T. Dekorsy, and K. Köhler, Femtosecond time-resolved optical pump-probe spectroscopy at kilohertz-scan-rates over nanosecond-time-delays without mechanical delay line, Appl. Phys. Lett. **88**, 041117 (2006).

[38] R. Gebs, G. Klatt, C. Janke, T. Dekorsy, and A. Bartels, High-speed asynchronous optical sampling with sub-50 fs time resolution, Opt. Express **18**, 5974 (2010).

[39] A. Bartels, R. Cerna, C. Kistner, A. Thoma, F. Hudert, C. Janke, and T. Dekorsy, Ultrafast time domain spectroscopy based on high-speed asynchronous optical sampling, Rev. Sci. Instrum. **78**, 035107 (2007).

[40] C. Waschke, P. Leisching, P. H. Bolivar, R. Schwedler, F. Brüggemann, H. G. Roskos, K. Leo, H. Kurz, and K. Köhler, Detection of Bloch oscillations in a semiconductor superlattice by time-resolved terahertz spectroscopy and degenerate four-wave mixing, Solid-State Electron. **37**, 1321 (1994).

[41] C. Waschke, H. G. Roskos, R. Schwedler, K. Leo, H. Kurz, and K. Köhler, Coherent Submillimeter-Wave Emission from Bloch Oscillations in a Semiconductor Superlattice, Phys. Rev. Lett. **70**, 3319 (1993).

[42] J. Floß, A. Kamalov, I. Sh. Averbukh, and P. H. Bucksbaum, Observation of Bloch Oscillations in Molecular Rotation, Phys. Rev. Lett. **115**, 203002 (2015).

[43] R. Sapienza, P. Costantino, D. Wiersma, M. Ghulinyan, C. J. Oton, and L. Pavesi, Optical Analogue of Electronic Bloch Oscillations, Phys. Rev. Lett. **91**, 263902 (2003).

[44] M. M. de Lima, Yu. A. Kosevich, P. V. Santos, and A. Cantarero, Surface Acoustic Bloch Oscillations, the Wannier-Stark Ladder, and Landau-Zener Tunneling in a Solid, Phys. Rev. Lett. **104**, 165502 (2010).

[45] V. Agarwal, J. A. del Río, G. Malpuech, M. Zamfirescu, A. Kavokin, D. Coquillat, D. Scalbert, M. Vladimirova, and B. Gil, Photon Bloch Oscillations in Porous Silicon Optical Superlattices, Phys. Rev. Lett. **92**, 097401 (2004).

[46] S. J. Pennycook and D. E. Jesson, High-resolution Z-contrast imaging of crystals, Ultramicroscopy **37**, 14 (1991).

[47] See Supplemental Material at http://link.aps.org/supplemental/10.1103/PhysRevMaterials.2.106002 for further details regarding the pump-probe reflectance experiments, the Fourier analysis of the results, and some additional simulations.

[48] M. F. Pascual-Winter, A. Fainstein, B. Jusserand, B. Perrin, and A. Lemaître, Spectral responses of phonon optical generation and detection in superlattices, Phys. Rev. B **85**, 235443 (2012).

[49] G. Rozas, M. F. Pascual Winter, B. Jusserand, A. Fainstein, B. Perrin, E. Semenova, and A. Lemaître, Lifetime of THz Acoustic Nanocavity Modes, Phys. Rev. Lett. **102**, 015502 (2009).

[50] C. Zener, A theory of the electrical breakdown of solid dielectrics, Proc. R. Soc. London A **145**, 523 (1934).

[51] L. Esaki and R. Tsu, Superlattice and negative differential conductivity in semiconductors, IBM J. Res. Dev. **14**, 61 (1970).

[52] J. Feldmann, K. Leo, J. Shah, D. A. B. Miller, J. E. Cunningham, T. Meier, G. von Plessen, A. Schulze, P. Thomas, and S. Schmitt-Rink, Optical investigation of Bloch oscillations in a semiconductor superlattice, Phys. Rev. B **46**, 7252 (1992).

[53] T. Dekorsy, R. Ott, H. Kurz, and K. Köhler, Bloch oscillations at room temperature, Phys. Rev. B **51**, 17275 (1995).

[54] H. Sanchis-Alepuz, Y. A. Kosevich, and J. Sánchez-Dehesa, Acoustic Analogue of Electronic Bloch Oscillations and Resonant Zener Tunneling in Ultrasonic Superlattices, Phys. Rev. Lett. **98**, 134301 (2007).

[55] A. Arreola-Lucas, G. Béez, F. Cervera, A. Climente, R. A. Méndez-Sanchez, and J. Sánchez-Dehesa, Mechanical rainbow trapping and Bloch oscillations in structured elastic beams, arXiv:1707.06558v2 [physics.app-ph]

Supplementary Information: Acoustic Confinement Phenomena in Oxide Multifunctional Nanophononic Devices

A. E. Bruchhausen,[1,2,*] N. D. Lanzillotti-Kimura,[1,3,†] B. Jusserand,[4] A. Soukiassian,[5] L. Xie,[6,7] X. Q. Pan,[7] T. Dekorsy,[2,8] D. G. Schlom,[5,9] and A. Fainstein[1]

[1] *Centro Atómico Bariloche & Instituto Balseiro (C.N.E.A.) and CONICET, 8400 S. C. de Bariloche, R. N., Argentina.*

[2] *Center for Applied Photonics and Department of Physics, University of Konstanz, D-78457 Konstanz, Germany.*

[3] *Centre de Nanosciences et de Nanotechnologies, C.N.R.S., Univ. Paris-Sud, Université Paris-Saclay, C2N Marcoussis, 91460 Marcoussis, France.*

[4] *Institut des NanoSciences de Paris, UMR 7588 C.N.R.S.-Université Pierre et Marie Curie, 75015 Paris, France.*

[5] *Department of Materials Science and Engineering, Cornell University, Ithaca, New York 14853, USA.*

[6] *National Laboratory of Solid State Microstructures and College of Engineering and Applied Sciences, Nanjing University, Nanjing 210093, P.R.China.*

[7] *Department of Chemical Engineering and Materials Science, University of California Irvine, Irvine, CA 92697, USA.*

[8] *Institute of Technical Physics, German Aerospace Center (DLR), Pfaffenwaldring 38-40, 70569 Stuttgart, Germany.*

[9] *Kavli Institute at Cornell for Nanoscale Science, Ithaca, New York 14853, USA.*

In this Supplemental Material we present additional figures and further details that serve as a complement to the data discussed in the main text. Section I shows examples of how the pump-probe reflectance experiments are performed, and how the contribution due to acoustic phonons is obtained. The detailed and complete Fourier analysis is explained in Section II. And finally, some simulation for related structures are presented in III.

* E-mail: axel.bruchhausen@cab.cnea.gov.ar

† E-mail: daniel.kimura@c2n.upsaclay.fr

I. PUMP-PROBE TRANSIENTS

The time-resolved pump-probe experiments measure the transient differential reflectivity $\frac{\Delta R(t)}{R_o}$, where R_o corresponds to the unperturbed reflectivity of the probe beam, i.e., before the arrival of the pump pulse. In Fig.S1 the measured transient signals for two samples are shown: panel a corresponding to the hybrid acoustic cavity and panel b corresponding to the hybrid acoustic molecule. The transients are characterized by a strong onset at $t = 0$ (defined by the simultaneous arrival at the sample of both the pump and the probe pulses), and the subsequent relaxation of the signal towards its steady-state condition. The observed temporal window of observation is defined by the inverse of the repetition rate of the pulsed laser, that is $f_R^{-1} = 1.25\,\text{ns}$. The evolution after the impulsive excitations is dominated by the electronic contribution to the modulation of the

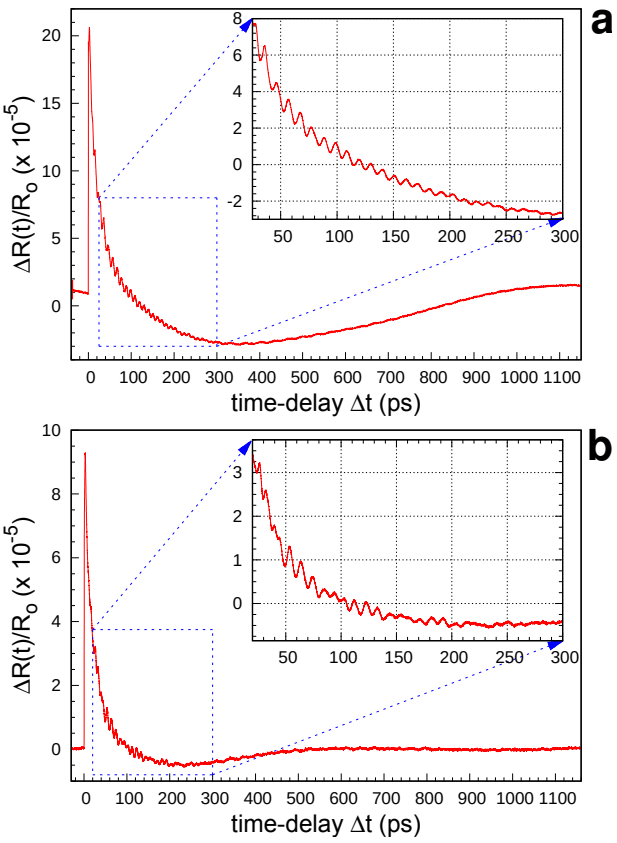

Figure S1: Time evolution of the transient differential pump-probe reflectivity ($\frac{\Delta R(t)}{R_o}$), as measured for two samples: **a)** corresponds to the hybrid acoustic cavity, and **b)** to the hybrid acoustic molecule. The insets show the detail of the oscillations due to the presence of acoustic phonons (shown in Fig. 2 of the main text).

optical constants. The main signal is modulated by weak high-frequency oscillations (see insets), which are in fact of central interest in this work, and corresponds to the modulation of the optical constants due to the presence of coherent acoustic phonons. The insets are a close up of the transients, where a clear difference in the temporal evolution of the high-frequency oscillations can be already distinguished between both samples. The experimental curves presented in Fig. 2 of the main text, are obtained by subtracting a fitted multi-exponential function (modelling the electronic diffusive-like contribution) to the measured transients.

II. FOURIER ANALYSIS

The spectral behaviour of the system under excitation is best observed by applying a Fourier transform. Figure S2 shows the Fourier analysis for the simple hybrid nanocavity (panel a) and the hybrid acoustic molecule (panel b). The left side displays the complete range of the numerical Fourier transform (nFT) of the extracted acoustic oscillations, i.e., both transients shown in of Fig.2 of the main text for the respective panels a) and b). The spectral features of interest are indicated by the stars, and are centred around 95 GHz. In panel a) a single peak corresponds to the confined acoustic mode (at ν ∼96 GHz). The spectral doublet (at ν_1 ∼85.9 GHz and ν_2 ∼101.5 GHz) in panel b) corresponding to the two coupled and confined modes of the hybrid acoustic molecule. The density plots at the left side display the windowed numerical Fourier transform (wnFT) of the transients using a sliding window of $\Delta T_{\text{wnft}} = 450$ ps, which enables a spectral resolution of about 2.2 GHz. The wnFT gives a glimpse of what the temporal evolution of each mode is. The confined mode, also in accordance with our simulations, for the case of the simple hybrid nanocavity displays a lifetime of about τ_ν ∼100 ps, while for the hybrid acoustic molecule both modes show practically the same lifetime of about $\tau_{\nu_1} \simeq \tau_{\nu_2}$ ∼90 ps.

Additional peaks are observed in the lower frequency region. These peaks correspond to the Brillouin modes [1] and are situated at ∼30 GHz (panel a) and ∼33 GHz (panel b). They mainly originate from the massive transparent substrate and the very small residual optical transmission of the metallic SRO layer. The substrate of both samples is different, explaining the different frequency at which these peaks appear. It is clear from the density plots, that the dynamics of these kind of modes is different from the cavity confined modes. Much weaker peaks at ∼24 GHz (panel a) and ∼26 GHz (panel b) are also observed, and correspond to Brillouin modes that result from the propagation of the stain pulse within the respective transparent STO/BTO acoustic Bragg mirrors (DBRs).

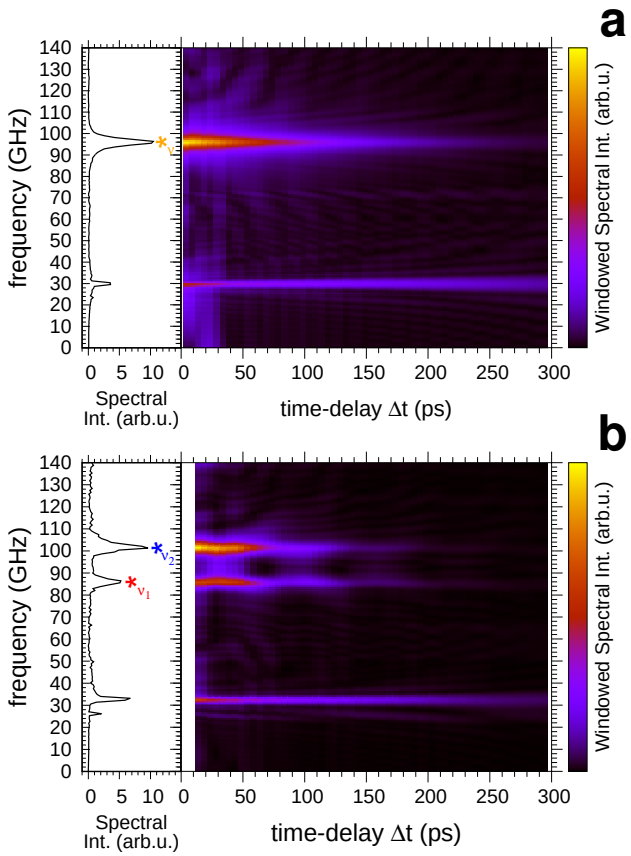

Figure S2: Fourier analysis of the transients acoustic oscillations for **a)** the hybrid acoustic nanocavity, and **b)** the phonon molecule, respectively, shown in Fig 2 a) and b) of the main text. The panels on the left show the numerical Fourier transform (nFT) of the transients and the panels on the right display the corresponding windowed numerical Fourier transform (wnFT) of the transient oscillations. The star ($*_\nu$) in panel **a)** indicates the presence of a single frequency corresponding to the cavity confined mode, whereas in **b)** the stars ($*_{\nu_1}$ and $*_{\nu_2}$) mark the two coupled modes of the phonon molecule. The spectral features in the lower frequency region correspond to Brillouin spectral modes, which result from the residual probe light that is transmitted into the highly transparent sample and substrate.

III. ADDITIONAL SIMULATIONS FOR RELATED STRUCTURES

In this section we present some additional simulations that complement and further understand the results shown in the main text.

First we analyse the structure corresponding to the hybrid acoustic molecule that consists of

two coupled acoustic cavities. In Fig.S3(top) a schematics of the structure is drawn, the effective $\lambda/2$ SRO/STO top cavity is coupled to the $\lambda/2$ BTO cavity by a *distributed Bragg reflector* (DBR) of N periods. $N = 1$ corresponds to the experimentally analysed sample. In S3(bottom) we show the simulation of the normalized absolute value of the surface displacement $|U(z = 0)|$ for varying number of periods N, from 1 to 8. As can be seen, for larger number of coupling periods, the

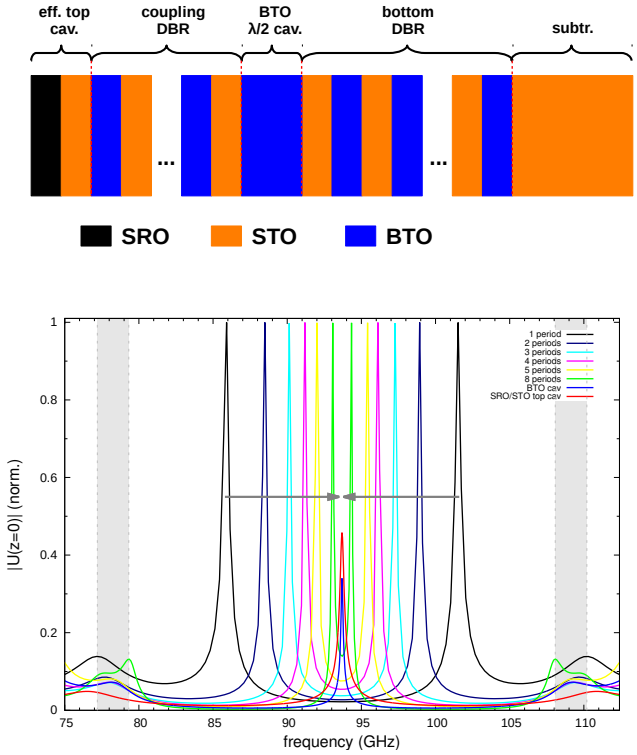

Figure S3: Hybrid acoustic molecule that consists of two coupled acoustic cavities. The simulations show the normalized absolute value of the surface displacement $|U(z = 0)|$ for varying number of periods of the coupling DBR. The shadowed areas indicate the approximate positions of the acoustic stop-band edges. The top panel presents the schematics of the structures.

coupling diminishes, and the peaks corresponding to the cavity modes shift towards each other (see grey arrows), tending to its uncoupled frequency. As a reference, with blue and red lines, the $|U(z = 0)|$ of the corresponding uncoupled (isolated) cavities, i.e. effective $\lambda/2$ SRO/STO top cavity and the $\lambda/2$ BTO top cavity, are respectively shown.

In Fig.S4, starting from the experimental hybrid acoustic molecule structure with one DBR coupling period ($N = 1$), we present simulations (bottom panel) varying the spacer width d_{BTO}

of the BTO cavity. Starting with $d_{BTO} = \lambda/4$, the whole structures corresponds to an effective $\lambda/2$ SRO/STO top cavity with a large DBR of 8.5×(BTO/STO) periods. d_{BTO} is increased up to $\lambda/4$ (experimental situation). As can be observed, the first structure has a mode centred at the acoustic stop band, and when d_{BTO} is increased, the original peak shifts to lower frequencies while the second mode arises from the upper DBR edge.

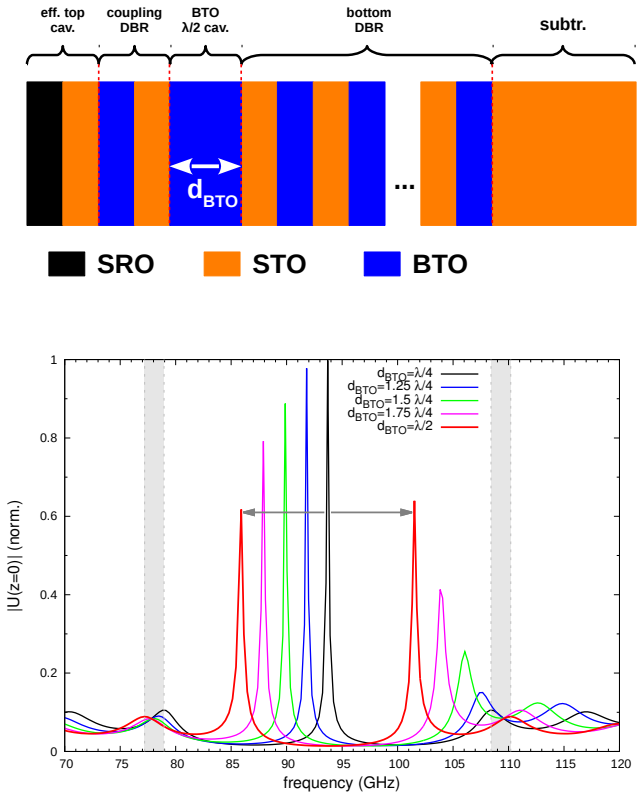

Figure S4: Evolution of the surface displacement of the two coupled acoustic cavities when the spacer width d_{BTO} of the BTO cavity is varied from $\lambda/4 \rightarrow \lambda/2$. The grey areas indicate the positions of the acoustic stop-band edges. The top panel presents the schematics of the structures.

In Fig.S5 a structure consisting of a $\lambda/2$ STO layer in-between two $\lambda/4$ BTO layers is considered. All three layers are embedded in STO. See the schematics of the structure in the top panel. The calculated acoustic reflectivity for waves arriving from one side is shown in the bottom panel (red curve). The dotted vertical line indicates the position of the modes frequency. This structure represents the simplest cavity structure based on acoustic impedance and interference phenomena. Both $\lambda/4$ BTO layers on each side of the STO cavity spacer, act as simple acoustic reflectors. For completeness, we also show the cases when additionally (BTO/STO) DBR periods are sym-

metrically added on both sides. The dashed curve corresponds to having added 2.5×(BTO/STO) periods on each side, and the full grey curve 5.5 periods. As can be observed, the modes position in frequency remains unchanged, but the mode becomes narrow and the stop-band increases its reflectivity and becomes better shaped and defined.

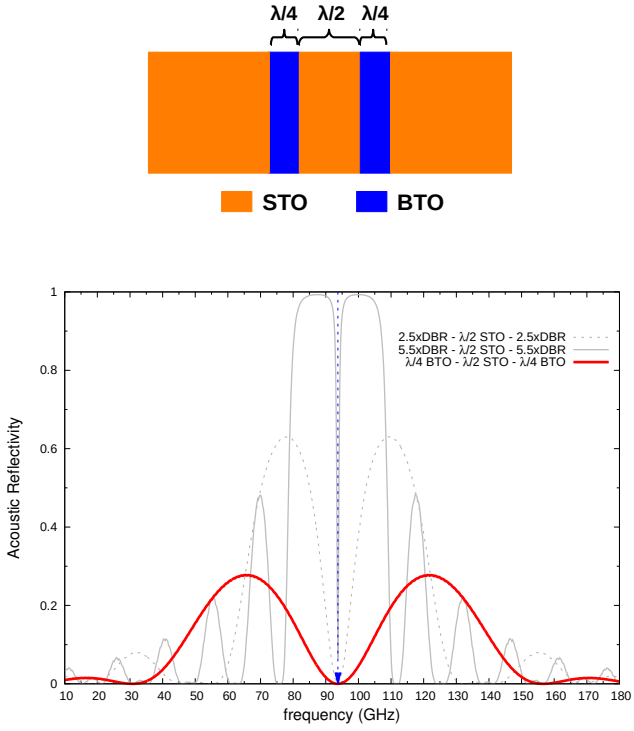

Figure S5: Acoustic reflectivity of an STO embedded $\lambda/4$ BTO-$\lambda/2$ STO-$\lambda/4$ BTO structure (see top panel for schematics), corresponding to a $\lambda/2$ STO acoustic cavity with a $0.5\times(BTO/STO)$ top/bottom DBR. The vertical dashed arrow indicates the acoustic confined mode. The reflectivity evolution for increasing number of DBR periods is depicted by the gray curves, as indicated.

Finally, we present an analysis of a hybrid acoustic top cavity, as the one presented in Sec. I of the main text, consisting of a $\lambda/2$ effective SRO/STO cavity spacer, with a bottom (BTO/STO) DBR (see Fig.S6 top panel for a schematic representation). The simulations shown in Fig.S6 (bottom panel) analyse the evolution of the surface displacement for varying number of periods N of the DBR: Starting from 0.5×(BTO/STO), corresponding to a single $\lambda/4$ BTO layer (red curve), that shows a broad mode. For increasing N, we see that the mode rapidly becomes narrower, and the acoustic stop-band becomes better shaped and better defined. The first case $N = 0.5$ is

somehow equivalent to the case analysed in Fig.S5.

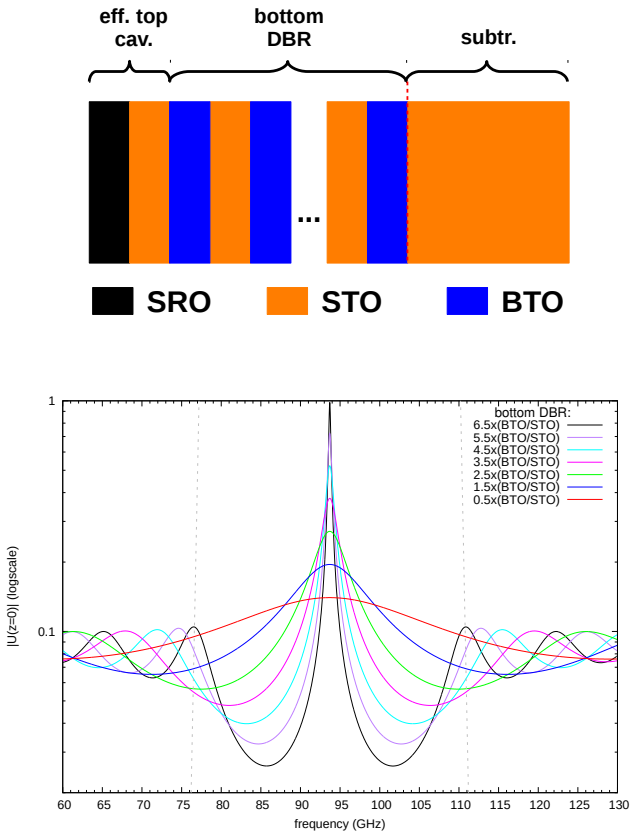

Figure S6: Hybrid acoustic top cavity. The schematic representation is shown in the top panel. Bottom panel: Surface displacement (log-scale) for varying number of periods of the bottom DBR, as indicated.

[1] C. Thomsen, J. Strait, Z. Vardeny, H. J. Maris, J. Tauc, and J. J. Hauser. *Phys. Rev. Lett.*, **53**, 989–992, (1984). Coherent Phonon Generation and Detection by Picosecond Light Pulses.